*Geochemistry, Geophysics, Geosystems*

Supporting Information for

# Anisotropy variations in the Alaska subduction zone based on shear-wave splitting from intraslab earthquakes

Cole Richards[1], Carl Tape[1], Geoffrey A. Abers[2], Zachary E. Ross[3]

[1]Geophysical Institute, University of Alaska Fairbanks, Fairbanks, Alaska, USA

[2]Department of Earth and Atmospheric Sciences, Cornell University, Ithaca NY

[3]Seismological Laboratory, California Institute of Technology, Pasadena CA

## Contents of this file

Anisotropy variations in the Alaska subduction zone based on shear-wave splitting from intraslab earthquakes

Cole Richards, Carl Tape, Geoffrey A. Abers, Zachary E. Ross

April 12, 2021

**Overview**

# S1 Analysis of teleseismic SKS shear wave splitting

SKS splitting has been extensively studied in Alaska and has been a scientific motivation for several temporary seismic deployments (Christensen & Abers, 2010; Hanna & Long, 2012; T.-R. A. Song & Kawakatsu, 2013; Perttu, Christensen, Abers, & Song, 2014; McPherson, Christensen, Abers, & Tape, 2020). We revisit SKS splitting measurements for three reasons:

1. to consider the largest possible selection of events in our region
2. to provide a consistent approach to measuring splitting of SKS and local S
3. to benchmark our SKS measurements with previous studies (McPherson et al., 2020)

## S1.1 Methods

The teleseismic dataset includes earthquakes from 2007-01-01 to 2017-12-31 recorded by SALMON, MOOS (Multidisciplinary Observations Of Subduction), TA, AVO, and the permanent network. All teleseismic data was pulled from the IRIS Data Management Center. In total there are 111 stations that were active for all or part of this period. The same region of interest used for the local S dataset was used here, and most of the stations are the same as well. The largest addition is that of MOOS (2006–2009) stations. MOOS provides dense station coverage on the Kenai Peninsula, especially the eastern portion, below which there is no mantle wedge. We include earthquakes with magnitudes $M_{\mathrm{w}} \geq 6.0$ occurring at epicentral distances between 80° and 140°, where the SKS-wave is isolated from other phases. SKS arrivals and ray paths were determined using TauP with velocity model scak (Table S1). The same measurement and quality control methods that were used for the local S splitting were applied to the SKS dataset except that here we filter for either 0.01–1 Hz or 0.02–1 Hz and use larger windows when making the measurement. Seismograms for 26,143 event station pairs were analyzed, resulting in 360 high-quality SKS splitting measurements. Figure S3 shows an example of a grade A SKS splitting measurement made at backarc SALMON station WFLS.

## S1.2 Results

Figure 7 shows all 360 grade A SKS measurements superimposed on a map of Cook Inlet as well as each measurement's ray traced through a cross section profile of the subduction zone. All of the map's features are the same as the local S splitting maps other than the delay time scale (length of bar, see legend) and the splitting measurement projection. The projection used here plots the splitting measurement at the surface directly above the 100 km depth point of the ray path. The 100 km depth point is shown as a green dashed line in the cross section profile. Again,

this is not to suggest that this is the depth where the anisotropic structure lies, but rather helps show coherent spatial patterns and back azimuthal dependence.

Due to the nature of teleseismic ray paths all the rays travel nearly vertically and this is seen in the ray tracing cross section of Figure 7. The most densely sampled region by the SKS measurements is the Kenai Peninsula where the slab dip is very shallow and there is no underlying mantle wedge. The steeply dipping section of the slab and mantle wedge above the 75–150 km slab depth contours is sparsely sampled. No SKS rays travel through the furthest corner mantle of the wedge/nose (50–75 km slab depth). The furthest back arc stations sparsely sample the mantle/wedge beyond where the slab depth reaches 200 km.

### S1.2.1 Classification of SKS splitting regions

We qualitatively define three regions containing different SKS splitting patterns (Figure 7). From west to east, these regions are:

- Region T1 has a majority of measurements with trench-perpendicular fast directions, but this region has the highest amount scatter. Region T1 does not have much overlap with the local regions.
- Region T2 displays a trench-parallel splitting pattern along with some scatter. Region T2 roughly aligns with region L1a, region L1b, and parts of region L2.
- Region T3, east of the ∼40 km subduction interface contour (Kenai Peninsula), contains most of the SKS measurements, and displays a strongly coherent plate-convergence-parallel splitting pattern. Region T3 roughly aligns with region L3.

The label T is a reminder that these classifications are based on teleseismic SKS data.

## S1.3 Discussion

The pattern in region T3 (see Section S1.2.1) has been observed in all the previous SKS studies in Alaska (Christensen & Abers, 2010; Hanna & Long, 2012; Perttu et al., 2014; Venereau, Martin-Short, Bastow, Allen, & Kounoudis, 2019; McPherson et al., 2020) and persists northwest toward the ∼70 km subduction interface contour in the flat slab region northwest of Cook Inlet. The ray paths in region T3 do not travel through the mantle wedge but rather have major parts in the subslab mantle and minor parts in the slab and overriding plate. Therefore, the splitting must be related to one or some combination of anisotropy beneath (T. A. Song & Kawakatsu, 2012; T.-R. A. Song & Kawakatsu, 2013) or within the subducting Pacific plate or structure in the overriding plate. This splitting pattern does not parallel the north-south magnetic lineations of the Pacific sea floor that we used as evidence to potentially attribute anisotropy in the slab to some of the trench-parallel local measurements. Furthermore, crustal contributions to SKS splitting are generally thought to be minimal (∼0.1 s) (Savage, 1999) whereas upper mantle contribution is much larger (∼ 1 s) (Silver, 1996; Fouch & Rondenay, 2006). Nearly all of the measurements here have $\delta t \geq 1$ s and some are longer than 2 s. The long delay times suggest that the main source of anisotropy is not in the overriding plate nor the lithosphere of the subducting slab. T. A. Song

and Kawakatsu (2012) show that oceanic asthenosphere characterized by weak azimuthal and strong radial anisotropy will have fast directions parallel to the plate motion direction where the slab dip is shallow. The long delay times, nearly horizontal slab, and parallel relationship between $\phi$ and the plate convergence direction suggest that the mostly likely source of anisotropy beneath region T3 is flow in the asthenosphere related to subduction of the Pacific plate (Figure S2a and b). However, we do not rule out contribution from the subducting lithosphere and overriding plate, especially because of the similar fast directions observed from local events (L3) in this region that do not sample subslab asthenosphere (Figures S7 and S2c).

Most measurements in region T2 are trench-parallel although there is some scatter in the fast directions. The most coherent trench-parallel pattern is seen south of the SALMON transect. The scatter increases to the north and is strongest at Spurr volcano (-152.25° 61.30°). The trench-parallel pattern is certainly less coherent in the Cook Inlet back arc for the SKS datasets in the study and previous studies (Figure 7). Previous SKS studies interpret trench-parallel flow in the mantle wedge here and for nearly all of the Alaska subduction zone, but seem to extrapolate this interpretation to Cook Inlet from the consistent trench-parallel fast directions in the adjacent backarcs (flat slab subduction region to the northeast and the Aleutians to the southwest) (McPherson et al., 2020; Venereau et al., 2019). The ray paths for region T2 travel through all components of the subduction system (overriding plate, mantle wedge/nose, subducting plate, and subslab mantle). Region T2 roughly corresponds to parts of regions L1a and L2 from the local splitting dataset. Just as previously discussed in local region L2, the trench-parallel splitting pattern can be explained by many different anisotropic sources. Both our local and SKS splitting results here could be explained by any combination of trench parallel anisotropy in the slab, along arc flow in the wedge, 2D corner flow with B-type olivine in the mantle nose, etc. 2D corner flow with B-type olivine in the mantle nose was suggested by the local splitting pattern in this region and could potentially contribute to the SKS splitting here. However, several measurements have significantly large delay times ($\delta t \geq 3s$) and this requires more anisotropy than can be found in the subducting slab, mantle wedge, and overriding plate. This emphasizes the importance of the subslab segment of the SKS ray path to these splitting observations. The anisotropy, at least for the larger delay times, likely lies in the subslab asthenosphere/mantle. This is fortified by results from region T3 suggesting strong anisotropy from flow in the subducting Pacific asthenosphere. The paradox in this interpretation is that the fast directions in regions T3 and T2 are nearly perpendicular to each other yet have the same source of anisotropy. This would mean that the fast directions in the subducting asthenosphere would need to change by 90° over a short distance. In region T2 the dip of the subducting slab is much steeper than in region T3. T. A. Song and Kawakatsu (2012) show that a change in slab dip can rotate the fast axis in the subslab asthenosphere by 90° with the assumption of a strong radial anisotropy component. Furthermore, T.-R. A. Song and Kawakatsu (2013) use this model to explain the sharp 90° transition of SKS splitting fast directions in the flat slab portion of the Alaska subduction zone. An important observation is that the sharp transition in SKS datasets is near the ∼75 km slab depth contour in the flat slab region and moves back to ∼50 km in Cook Inlet. The transition in Cook Inlet is less prominent in our dataset compared to the previous SKS studies, but appears to exist at ∼50 km as well (Figure 7). The slab dip is steeper in Cook Inlet and thus T. A. Song and Kawakatsu (2012) would predict the sharp change in splitting pattern to occur closer to the trench than in

the flat slab region. This is exactly what the jump in splitting transition from ∼75 km to ∼50 km in the SKS datasets show. Therefore, we agree with T.-R. A. Song and Kawakatsu (2013) and interpret the splitting pattern observed in region T2 to have main contributions from flow in the dipping subslab asthenosphere related to Pacific plate motion (Figure S2a). We also expect minor contributions from anisotropy in the subducting lithosphere and mantle wedge. Any wedge and lithospheric contribution in region T2 would be corroborated by our local splitting results and the notable number of trench-perpendicular measurements all SKS datasets.

Region T1 has ray paths that are strictly in the mantle wedge and overriding plate. While the splitting pattern here is complex, the longest splits and majority of the splits are roughly trench-perpendicular. Leaning on the strong evidence of trench-perpendicular anisotropy from 2D corner flow in the mantle wedge that was observed in the local dataset, we attribute the trench-perpendicular SKS measurements here to the same 2D corner flow. We favor a change in dip of the subslab asthenospheric flow (T.-R. A. Song & Kawakatsu, 2013) to explain the transition from plate convergence parallel fast directions in region 1 to trench-parallel fast directions in region 2. However, as was discussed in the local splitting section, we do not rule out potential contributions to trench-parallel splitting from B-type olivine in the mantle nose. Finally, we do not dispute trench-parallel flow in the wedge near the slab edge but our study region is too far away from the edge to see significant influence of this flow (T.-R. A. Song & Kawakatsu, 2013; Venereau et al., 2019).

## S2 Spatial smoothing of splitting measurements

Our procedure for spatial smoothing is as follows:

1. Define each splitting measurement as a complex number $z = r\, e^{i\alpha}$, where $r$ is the magnitude ($\delta t$) and $\alpha$ is the polar angle (counterclockwise from east).

2. Calculate $z^2 = r^2\, e^{i2\alpha}$ and define $Z = z^2 = A + iB$.

3. Since $z$ vary with colatitude $\theta$ and longitude $\phi$, we have $Z(\theta, \phi) = A(\theta, \phi) + iB(\theta, \phi)$.

4. Apply a multiscale spherical wavelet estimation procedure (Tape, Musé, Simons, Dong, & Webb, 2009; Tape, Plesch, Shaw, & Gilbert, 2012) to obtain the spatially continuous scalar functions $A'(\theta, \phi)$ and $B'(\theta, \phi)$, which in turn give $Z'(\theta, \phi)$, where the prime-notation denotes an estimated quantity.

   For our dataset we used spherical grid orders $q = 6, 7$, and 8 to estimate the continuous functions.

5. Evaluate $Z'(\theta, \phi)$ at the input values of $(\theta, \phi)$ and convert back to $r'$ and $\alpha'$.

## References


Argus, D. F., Gordon, R. G., & DeMets, C. (2011). Geologically current motion of 56 plates relative to the no-net-rotation reference frame. *Geochem. Geophy. Geosyst.*, *12*, 1–13. doi: 10.1029/2011GC003751

Becker, T. W., Schaeffer, A. J., Lebedev, S., & Conrad, C. P. (2015). Toward a generalized plate motion reference frame. *Geophys. Res. Lett.*, *42*, 3188–3196. doi: 10.1002/2015GL063695

Christensen, D. H., & Abers, G. A. (2010). Seismic anisotropy under central Alaska from SKS splitting observations. *J. Geophys. Res.*, *115*. doi: 10.1029/2009JB006712

Doubrovine, P. V., Steinberger, B., & Torsvik, T. H. (2012). Absolute plate motions in a reference frame defined by moving hot spots in the Pacific, Atlantic, and Indian oceans. *J. Geophys. Res.*, *117*, 1–30. doi: 10.1029/2011JB009072

Fogleman, K. A., Lahr, J. C., Stephens, C. D., & Page, R. A. (1993). *Earthquake locations determined by the southern Alaska Seismograph Network for October 1971 through May 1989.* U.S. Geol. Survey. (Open-File Report 93-309, v. 1.1)

Fouch, M., & Rondenay, S. (2006, 10). Seismic anisotropy beneath stable continental interiors. *Physics of the Earth and Planetary Interiors*, *158*, 292-320. doi: 10.1016/j.pepi.2006.03.024

Hanna, J., & Long, M. D. (2012). SKS splitting beneath Alaska: Regional variability and implications for subduction processes at a slab edge. *Tectonophysics*, *530-531*, 272–285.

Hayes, G. P., Moore, G. L., Portner, D. E., Hearne, M., Flamme, H., Furtney, M., & Smoczyk, G. M. (2018). Slab2, a comprehensive subduction zone geometry model. *Science*, *362*, 58–61. doi: 10.1126/science.aat4723

Matumoto, T., & Page, R. A. (1969). Microaftershocks following the Alaska earthquake of March 28, 1964: Determination of hypocenters and crustal velocities in the Kenai Peninsula-Prince William Sound area. In L. E. Leipold & F. J. Wood (Eds.), *The prince william sound, alaska, earthquake of 1964 and aftershocks* (Vols. II, Parts B and C, pp. 157–173). Washington, D.C.: U.S. Department of Commerce, Environmental Science Services Administration. (U.S. Coast and Geodetic Survey Publication 10-3)

McPherson, A. M., Christensen, D. H., Abers, G. A., & Tape, C. (2020). Shear wave splitting and mantle flow beneath Alaska. *J. Geophys. Res. Solid Earth*, *123*, 1–18. doi: 10.1029/2019JB018329

Miller, M. S., & Moresi, L. (2018). Mapping the Alaska Moho. *Seismol. Res. Lett.*, *89*(6), 2430–2436. doi: 10.1785/0220180222

Morgan, W. J., & Morgan, J. P. (2007). Plate velocities in the hotspot reference frame. In G. R. Foulger & D. M. Jurdy (Eds.), *Plates, plumes, and planetary processes* (pp. 65–78). Boulder, Colo., USA: Geol. Soc. Am. (Special Paper 430)

Perttu, A., Christensen, D., Abers, G., & Song, X. (2014). Insights into mantle structure and flow beneath Alaska based on a decade of observations of shear wave splitting. *J. Geophys. Res. Solid Earth*, *119*, 8366–8377. doi: 10.1002/2014JB011359

Savage, M. K. (1999). Seismic anisotropy and mantle deformation: What have we learned from shear wave splitting. *Rev. Geophys.*, *37*(1), 65–106.

Silver, P. G. (1996). Seismic anisotropy beneath the continents: Probing the depths of geology. *Annual Review of Earth and Planetary Sciences*, *24*(1), 385-432. Retrieved from `https://doi.org/10.1146/annurev.earth.24.1.385` doi: 10.1146/annurev.earth.24.1.385

Song, T. A., & Kawakatsu, H. (2012). Subduction of oceanic asthenosphere: Evidence from sub-slab seismic anisotropy. *Geophys. Res. Lett.*, *39*. doi: 10.1029/2012GL052639

Song, T.-R. A., & Kawakatsu, H. (2013). Subduction of oceanic asthenosphere: A critical appraisal in central Alaska. *Earth Planet. Sci. Lett.*, *367*, 82–94.

Tape, C., Musé, P., Simons, M., Dong, D., & Webb, F. (2009). Multiscale estimation of GPS velocity fields. *Geophys. J. Int.*, *179*, 945–971. doi: 10.1111/j.1365-246X.2009.04337.x

Tape, C., Plesch, A., Shaw, J. H., & Gilbert, H. (2012). Estimating a continuous Moho surface for the California Unified Velocity Model. *Seismol. Res. Lett.*, *83*(4), 728–735.

Venereau, C. M. A., Martin-Short, R., Bastow, I. D., Allen, R. M., & Kounoudis, R. (2019). The role of variable slab dip in driving mantle flow at the eastern edge of the Alaskan subduction margin: insights from SKS shear-wave splitting. *Geochem. Geophy. Geosyst.*, *20*, 2433-2448. doi: 10.1029/2018GC008170

Table S1: 1D structural model `scak` used for calculating incidence angles, SKS arrivals, and ray tracing. For all depths below 66 km the model we use is identical to `ak135`. This is the 1D model used by the Alaska Earthquake Center for locating earthquakes south of 62.5° latitude (Matumoto & Page, 1969; Fogleman et al., 1993).

| top of layer, km | bottom of layer, km | thickness km | $V_S$ m/s | $V_P$ m/s | density kg/m$^3$ | $Q_S$ | $Q_P$ |
|---|---|---|---|---|---|---|---|
| 0 | 4 | 4 | 3010 | 5300 | 2520 | 300 | 600 |
| 4 | 9 | 5 | 3180 | 5600 | 2610 | 300 | 600 |
| 9 | 14 | 5 | 3520 | 6200 | 2780 | 300 | 600 |
| 14 | 19 | 5 | 3920 | 6900 | 2970 | 300 | 600 |
| 19 | 24 | 5 | 4200 | 7400 | 3120 | 300 | 600 |
| 24 | 33 | 9 | 4370 | 7700 | 3200 | 300 | 600 |
| 33 | 49 | 16 | 4490 | 7900 | 3260 | 300 | 600 |
| 49 | 66 | 17 | 4600 | 8100 | 3320 | 300 | 600 |
| 66 | – | – | 4720 | 8300 | 3370 | 300 | 600 |

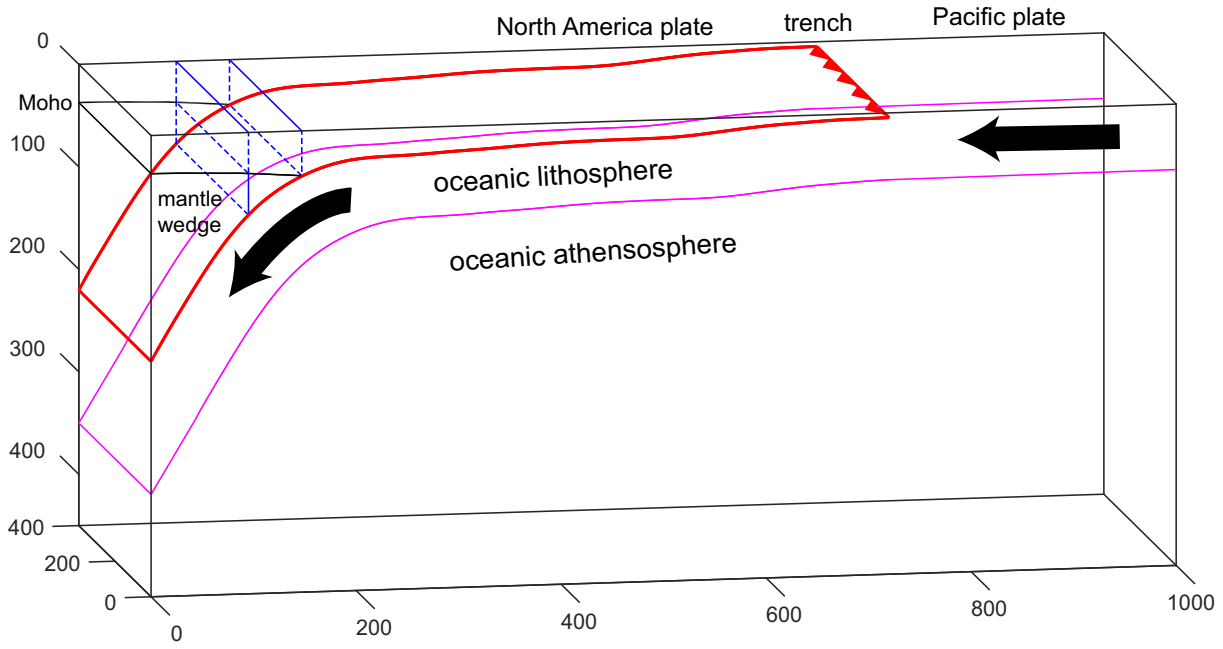


Figure S1: Cross section of the Cook Inlet segment of the Alaska subduction zone along the profile shown in Figure 2. The slab geometry is slab2.0 (Hayes et al., 2018), and the Moho geometry is from Miller and Moresi (2018). The left portion is examined in Figure S2.

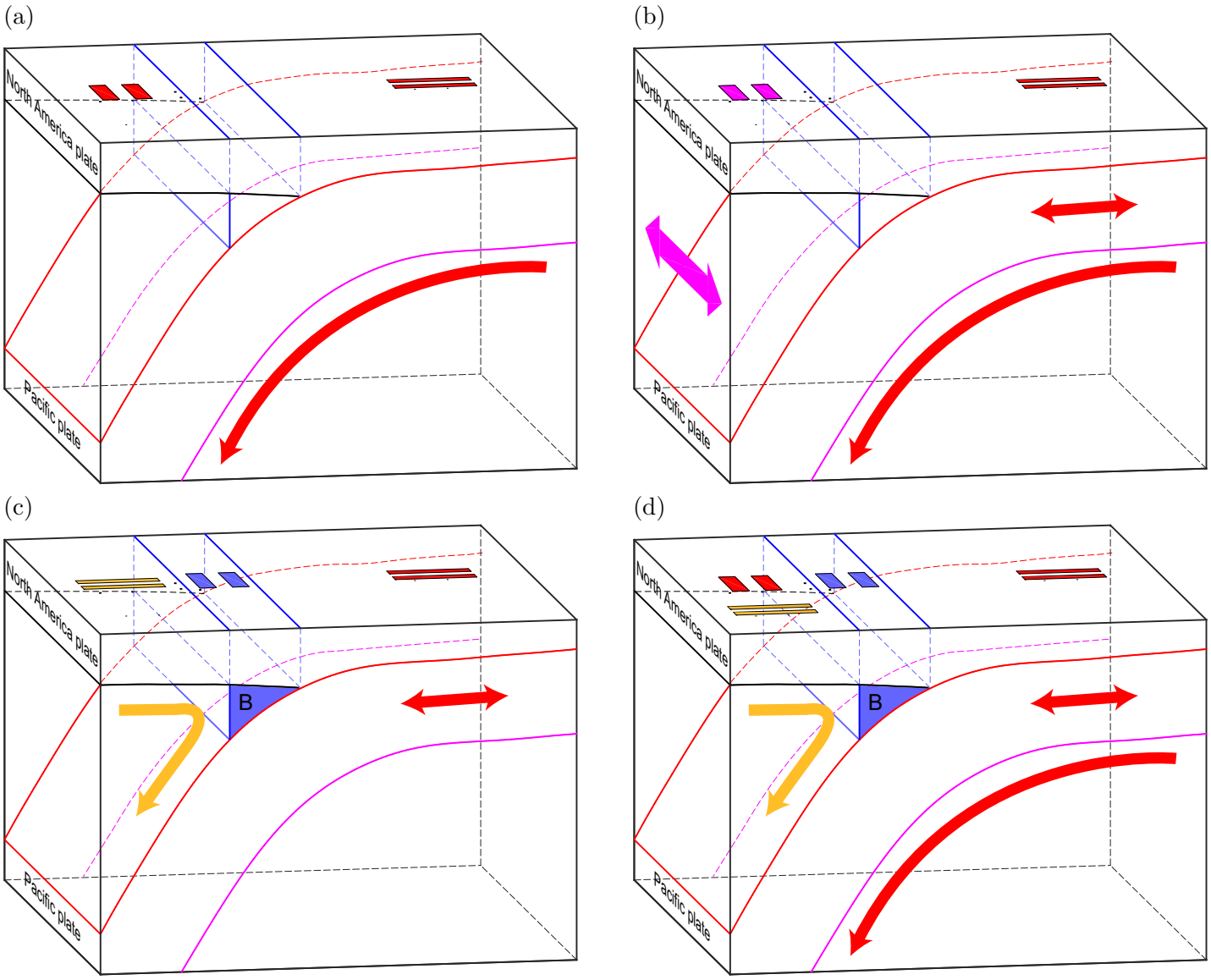


Figure S2: Four different interpretations of flow and anisotropy, based on local S and SKS shear-wave splitting measurements. The domain is a shortened version of what is shown in Figure S1. The overlying bars represent splitting observations that correspond to the anisotropy of the color-coded arrows in the various components of the subduction cartoon. The bottom of the mantle nose ("B") is drawn at the 80 km depth of the Pacific plate. (a) Interpretation of SKS splitting measurements, from T.-R. A. Song and Kawakatsu (2013). (b) Interpretation of SKS splitting measurements, from Christensen and Abers (2010) (c) Interpretation of local splitting measurements from this study. (d) Our overall favored model to explain both the local S and SKS splitting patterns.

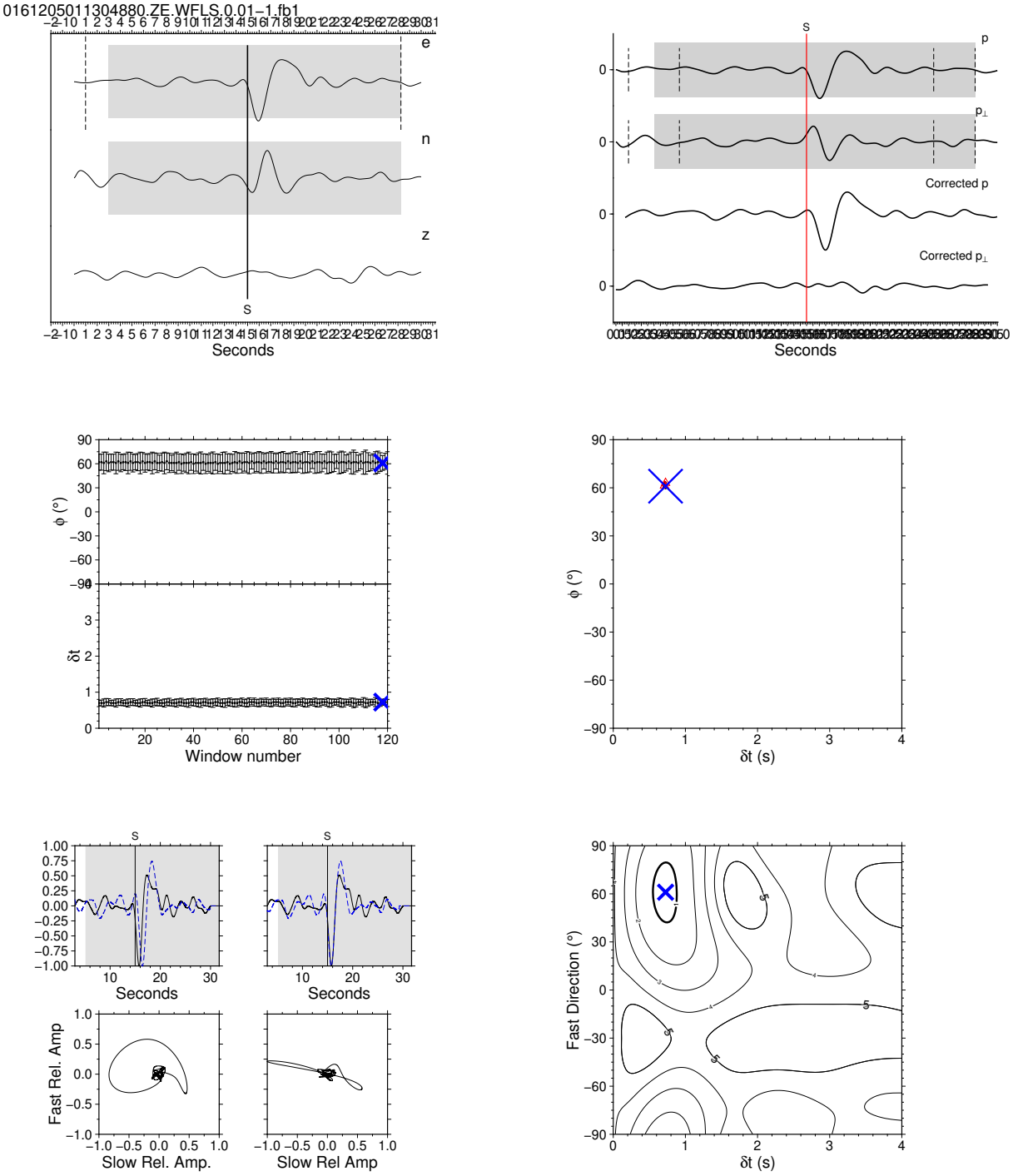


Figure S3: Same as Figure 3 but for an SKS splitting measurement.

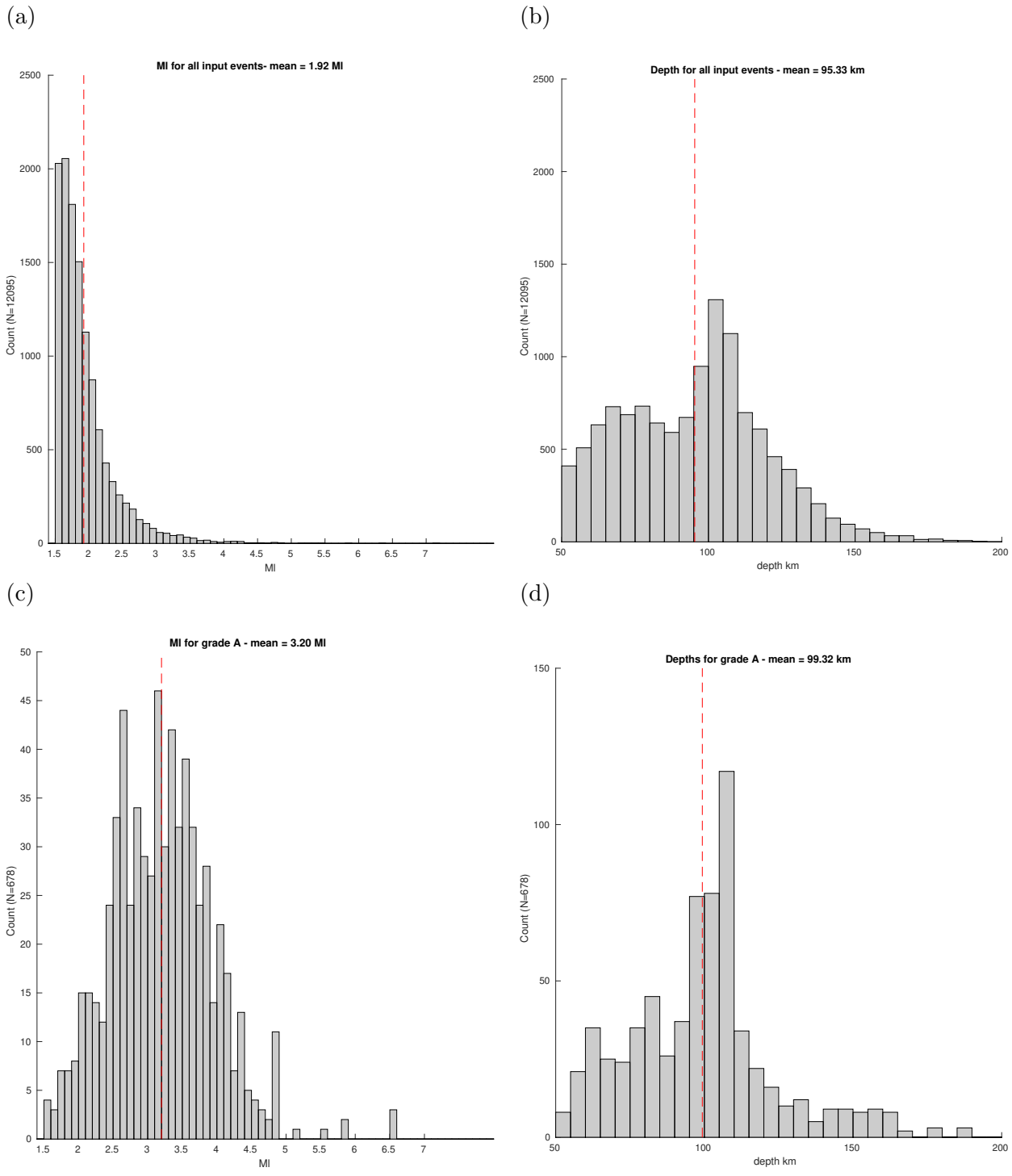


Figure S4: Distributions of magnitude and depths for input events and the 'final' events for which there was at least one high-quality local S splitting measurement (high SNR, low uncertainty in $\phi$, unique solution, and incidence angles $\leq 37°$). Here, all events have depths $\geq$50 km. Vertical red dashed line marks the mean. (a) $M_l$ for input events. (b) Depth for input events. (c) $M_l$ for final events (n=678). (d) Depth for final events (n=678).

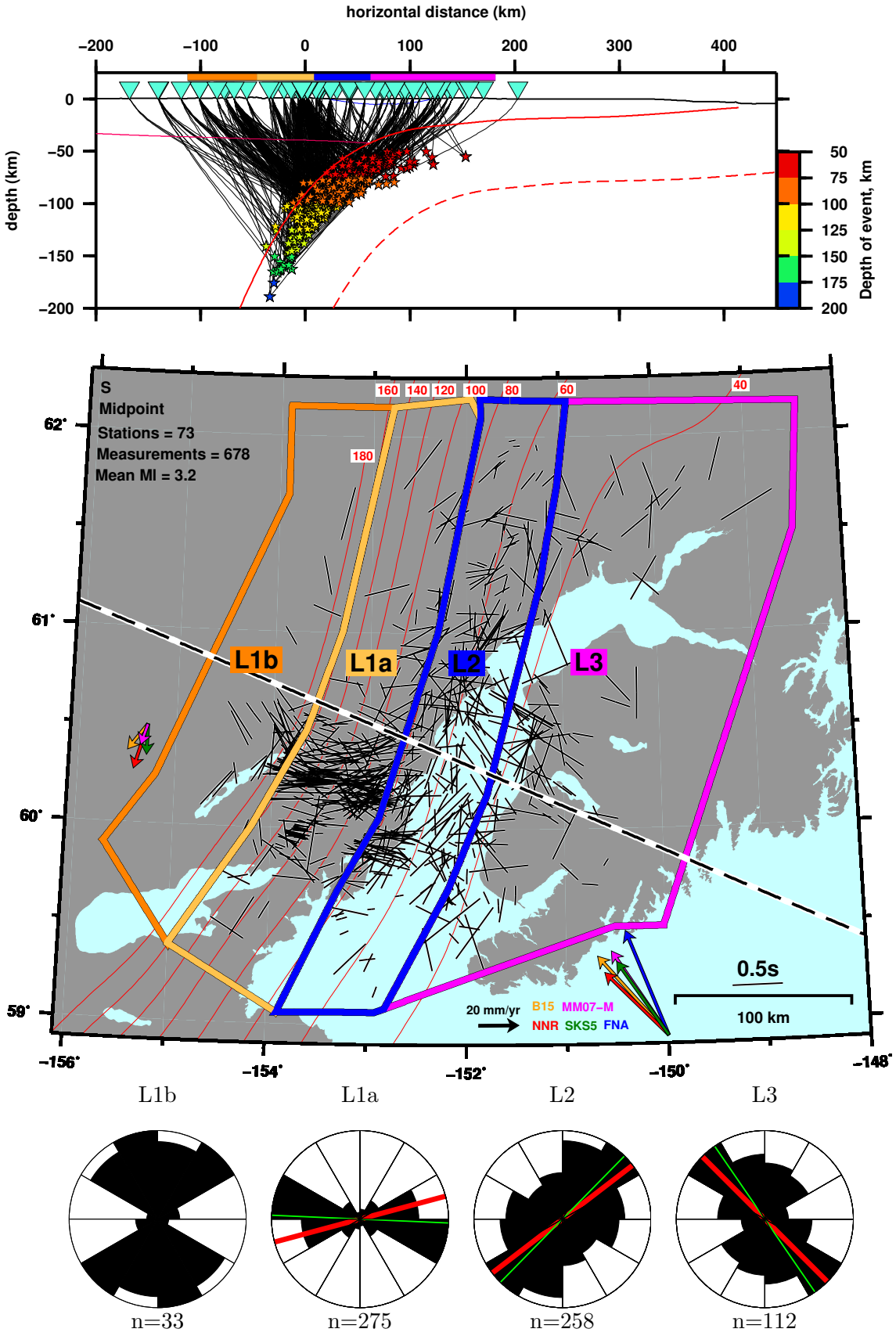


Figure S5: [caption on following page]

Figure S5 caption: Splitting measurements from local intraslab earthquakes in this study. (top) Ray paths for all measurements, projected into the cross section shown as the dashed line. Red solid line is the subduction interface (Hayes et al., 2018). Magenta line is the continental Moho (Miller & Moresi, 2018). Inverted triangles are stations. Stars are earthquakes colored by depth. Black lines leading from event to station are ray paths. Dashed red line is the approximate bottom of the subducting oceanic lithosphere. (middle) All local splitting measurements, with each displayed at the midpoint between station and event. Each measurement is plotted as a black bar with its orientation parallel to $\phi$ and length scaled to $\delta t$. Red contours indicated the depth to the subduction interface and range from 40 km to 180 km. Black and white dashed line represents the cross section seen above. Plate motion vectors: B15 (yellow) spreading alignement (Becker, Schaeffer, Lebedev, & Conrad, 2015), MM07-M (magenta) modified hotspot (Morgan & Morgan, 2007; Doubrovine, Steinberger, & Torsvik, 2012), NNR (red) no-net-rotation MORVEL (Argus, Gordon, & DeMets, 2011), SKS5 (green) SKS shear-wave splitting (Becker et al., 2015), FNA (blue) fixed North America in MORVEL (Argus et al., 2011). The interpreted splitting regions from west to east, are: L1b (orange), L1a (yellow), L2 (blue), and L3 (magenta). (bottom) Rose diagrams for the splitting regions. The red line is the mean fast direction weight by delay time, the green line is the mean fast direction without weighting by delay time.

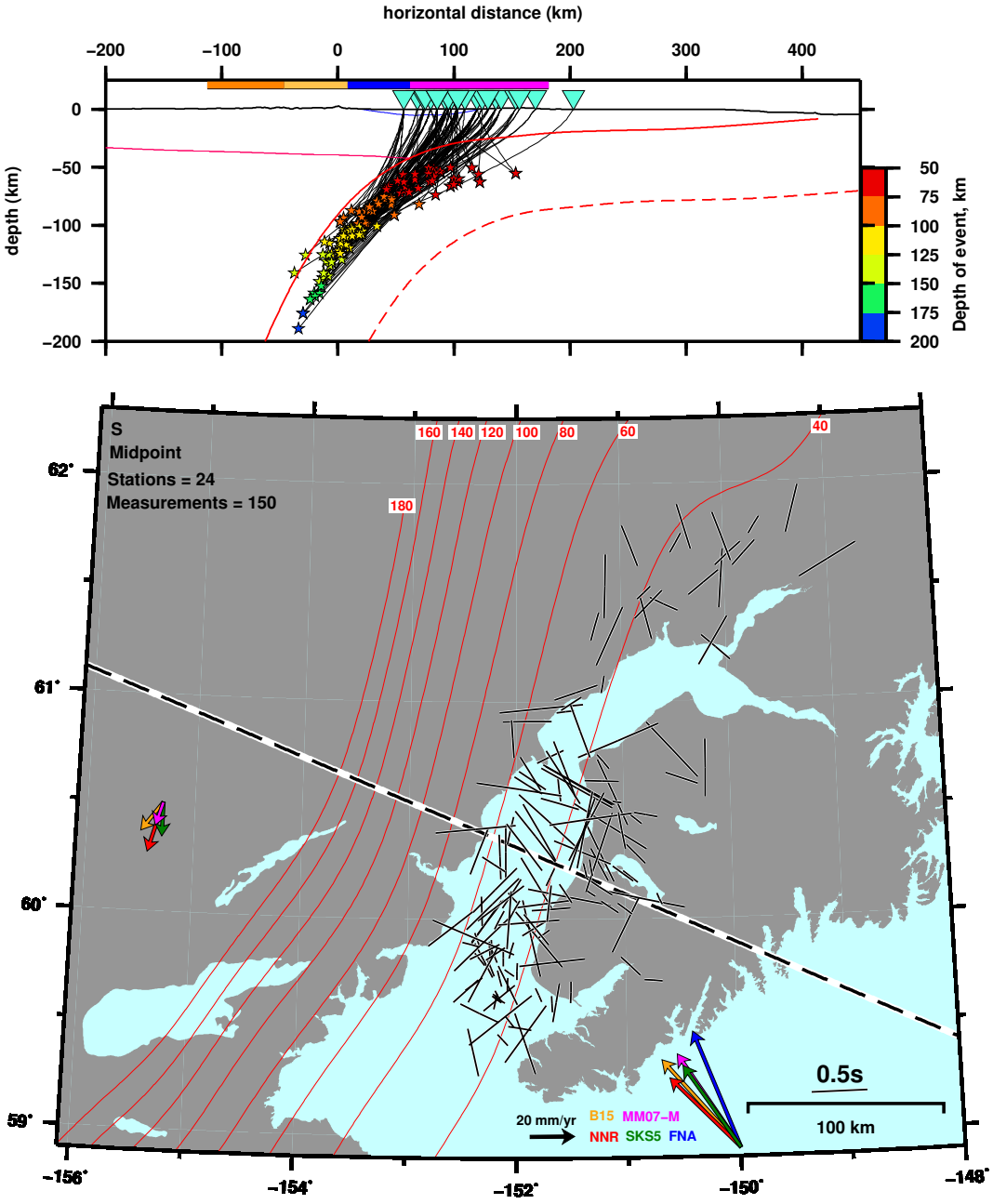


Figure S6: Local splitting measurements (midpoint projection) for events to all stations that have most of their ray paths in the slab. While there seems to be some coherence in the north, the splitting pattern is complex. The overall large delay times suggest that the slab is anisotropic.

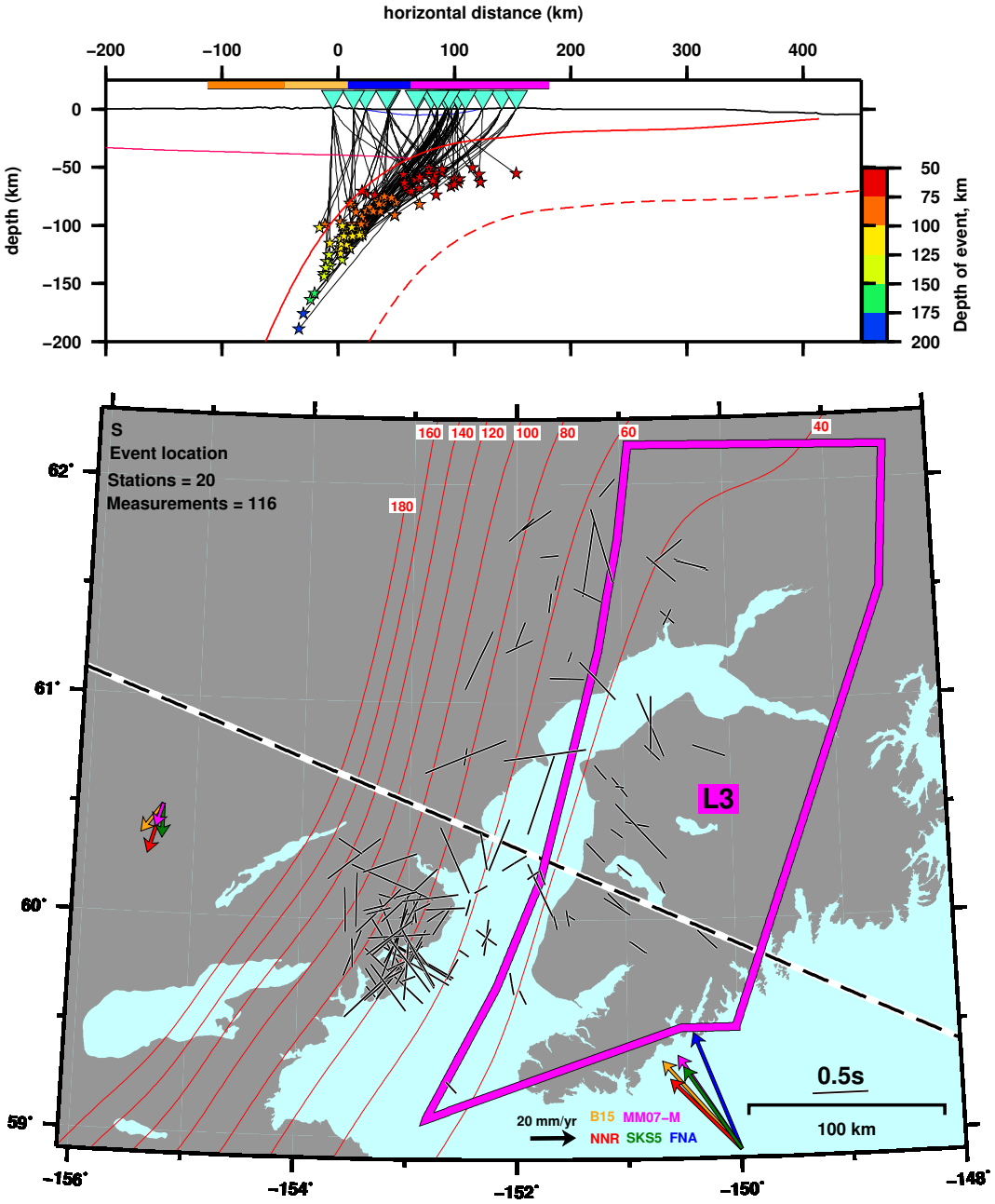


Figure S7: Local splitting measurements (event location) for stations with events originating under the Kenai Peninsula. Note the consistent northwest–southeast splitting pattern for the Kenai Peninsula. This patterns matches well with SKS splitting from this study and previous studies.

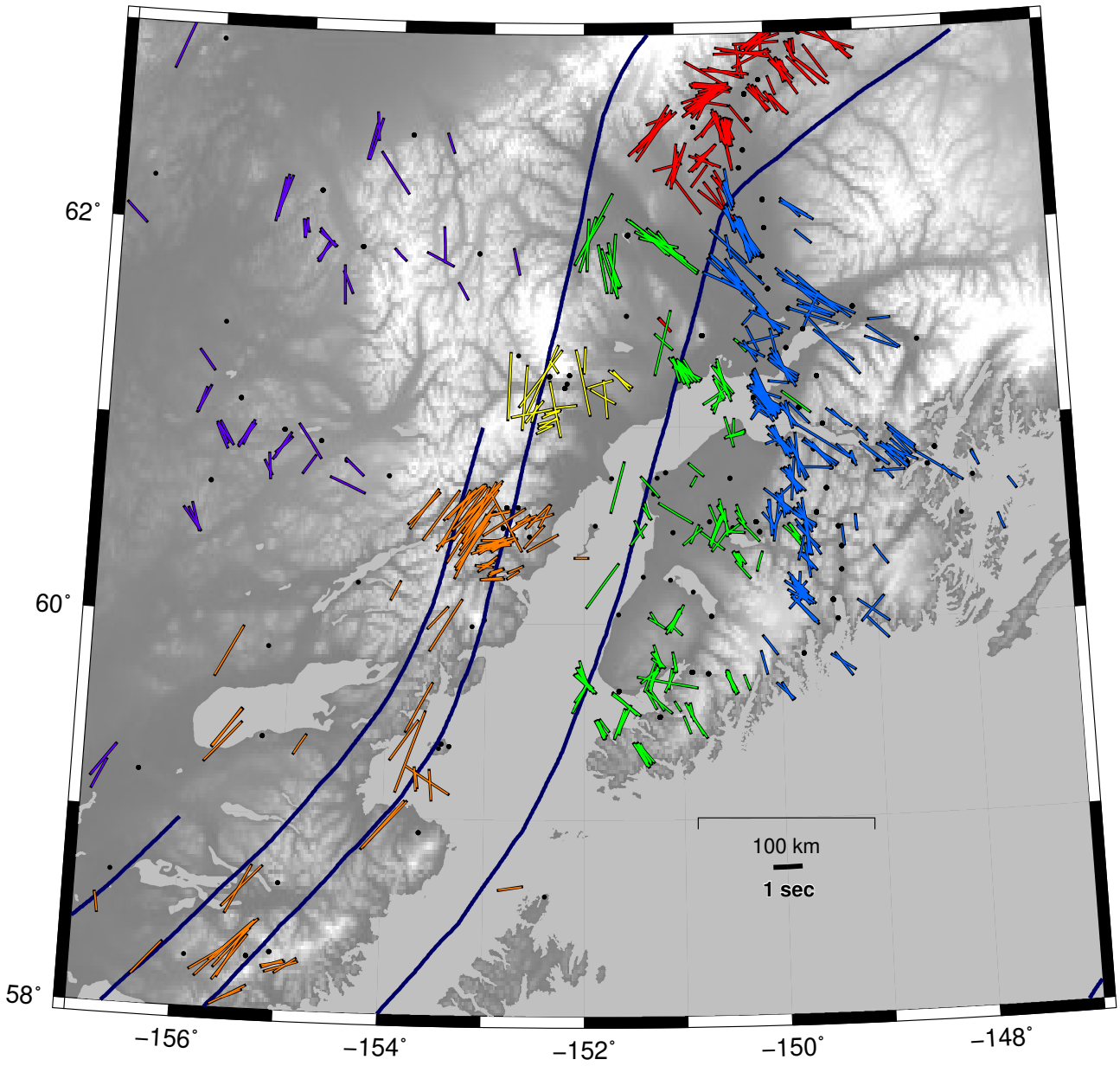


Figure S8: McPherson et al. (2020) SKS splitting observations plotted at the 100 km projection of the rays paths. The thick blue lines show the depth of the subducting slab at 50, 100, 150, and 200 km depth. Dots indicate station locations.

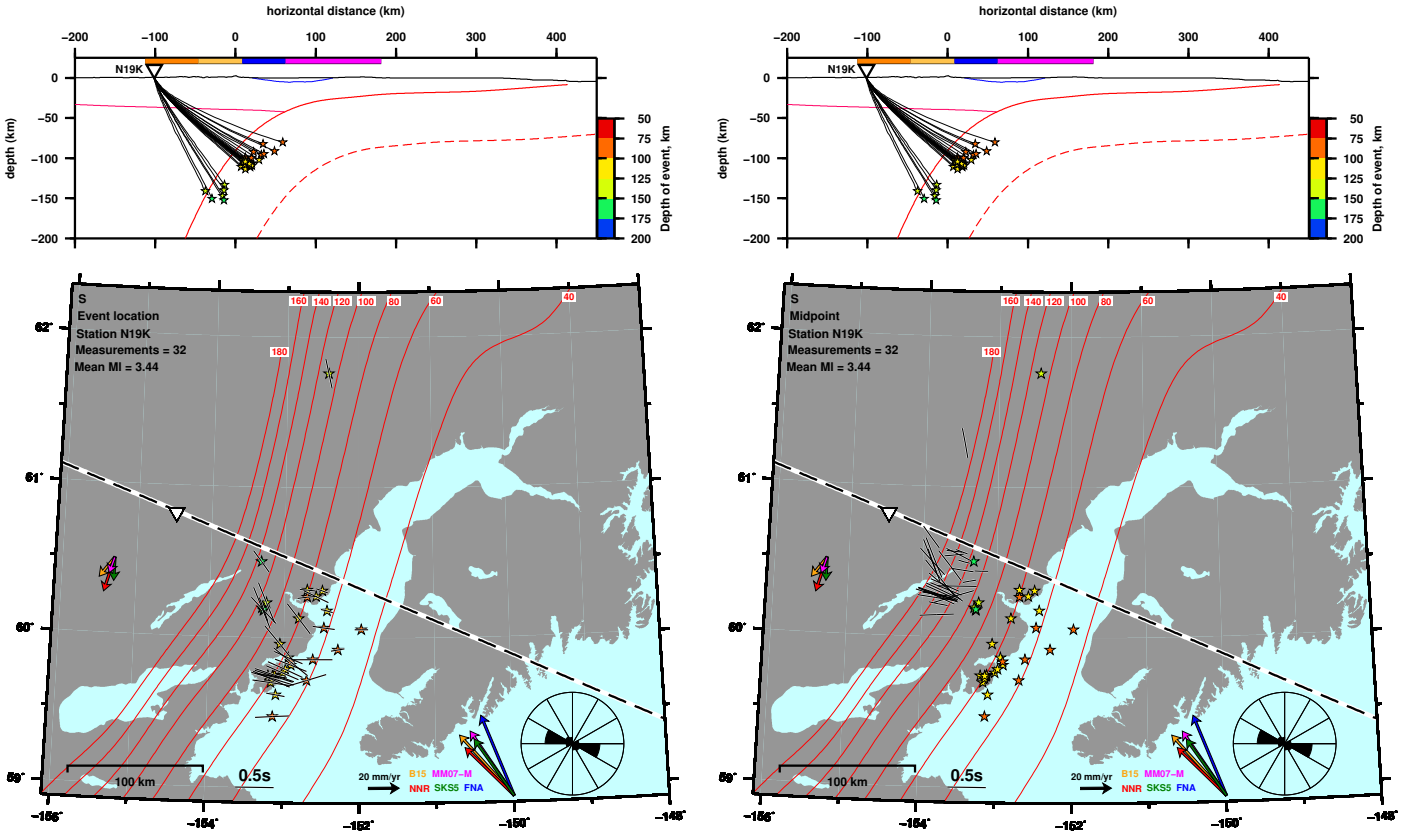


Figure S9: TA.N19K: Example station 1 out of 5 from west to east on the Redoubt line. N19K displays a trench-perpendicular splitting pattern with convergence parallel measurements for the deepest events. Splitting measurements are plotted at the event location (left) or midpoint projection (right)

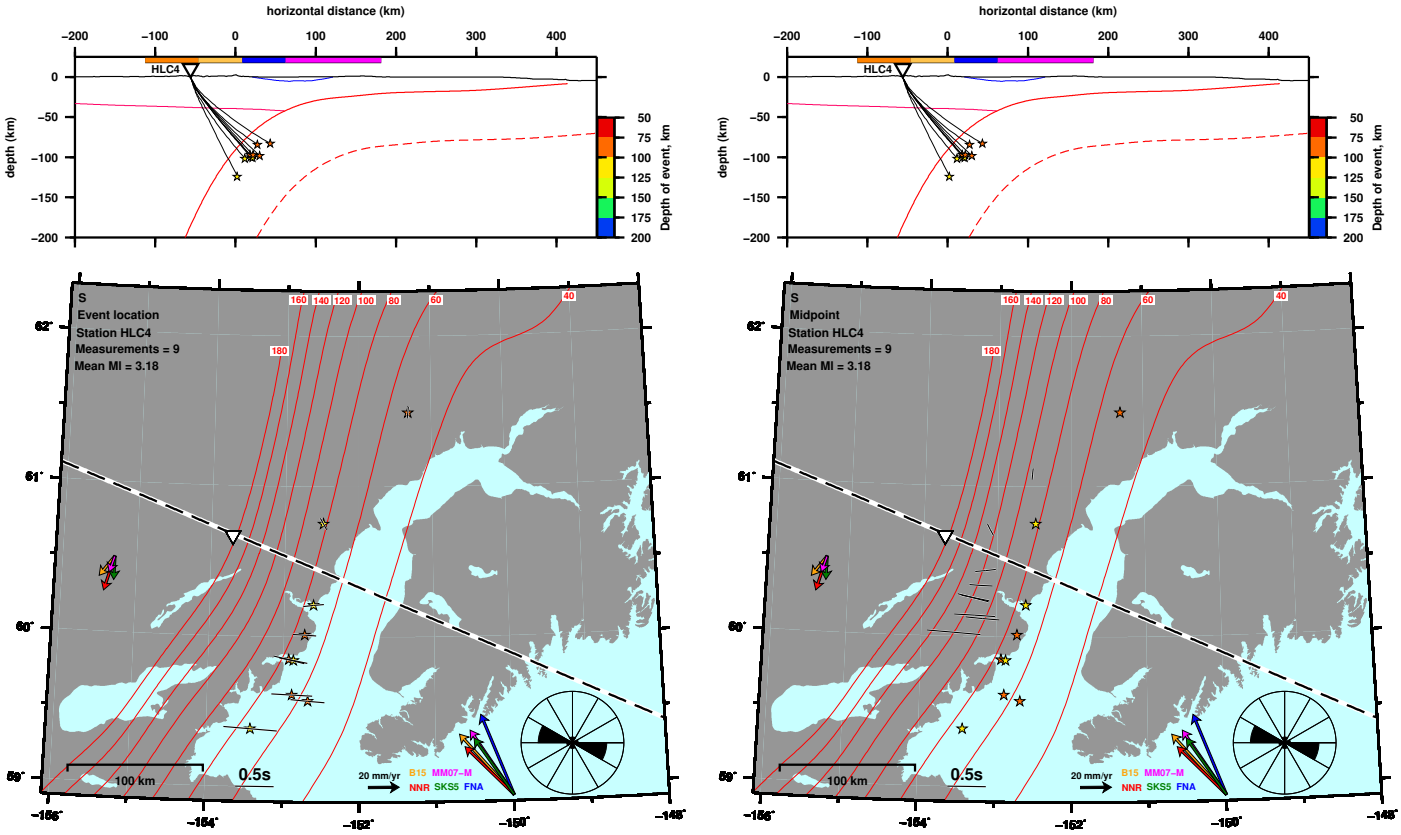


Figure S10: ZE.HLC4: Example station 2 out of 5 from west to east on the Redoubt line. HLC4 displays a trench-perpendicular splitting pattern. Splitting measurements are plotted at the event location (left) or midpoint projection (right)

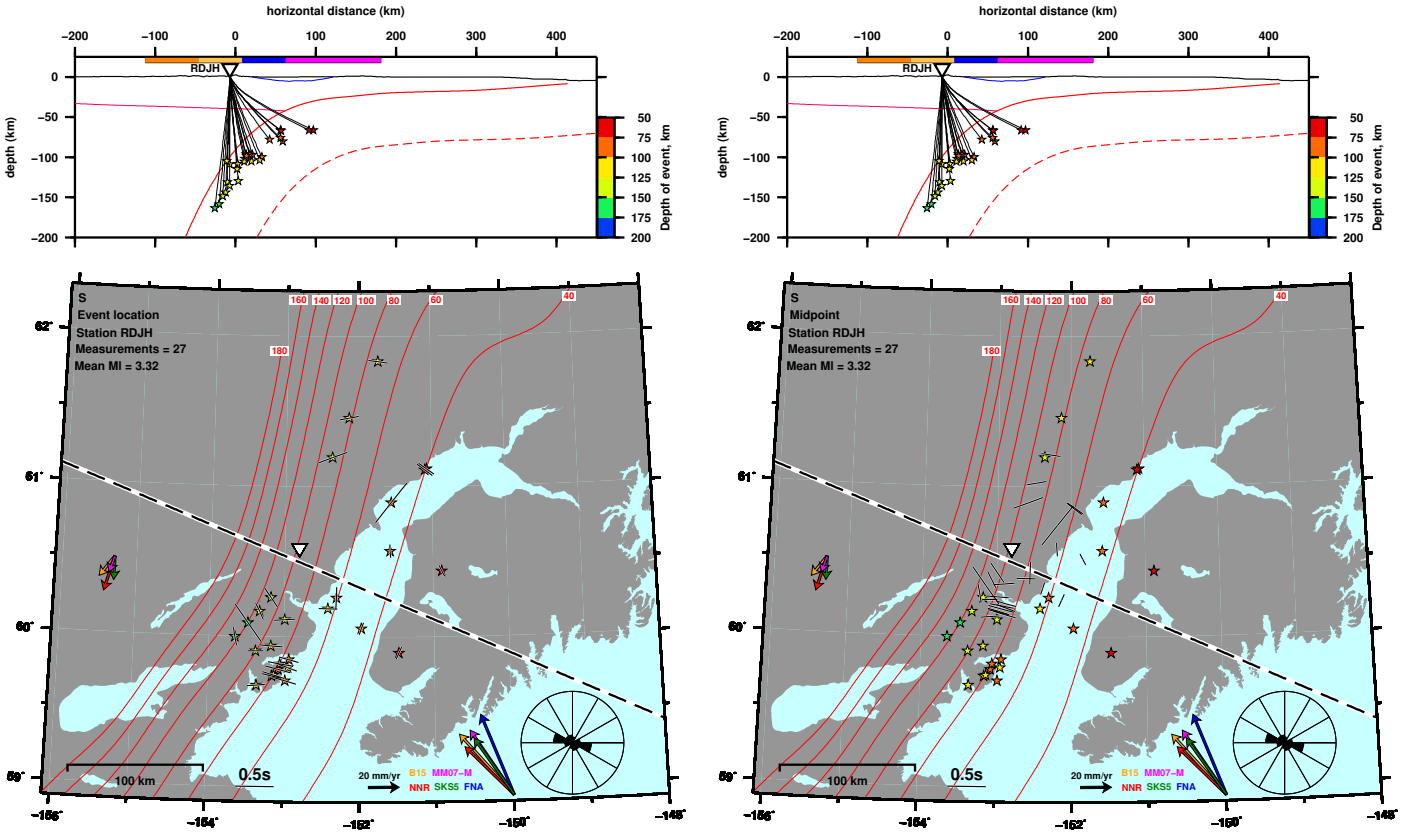


Figure S11: AV.RDJH: Example station 3 out of 5 from west to east on the Redoubt line. RDJH displays coherent patterns from each splitting region (L1b,L1a,L2,L3). Splitting measurements are plotted at the event location (left) or midpoint projection (right)

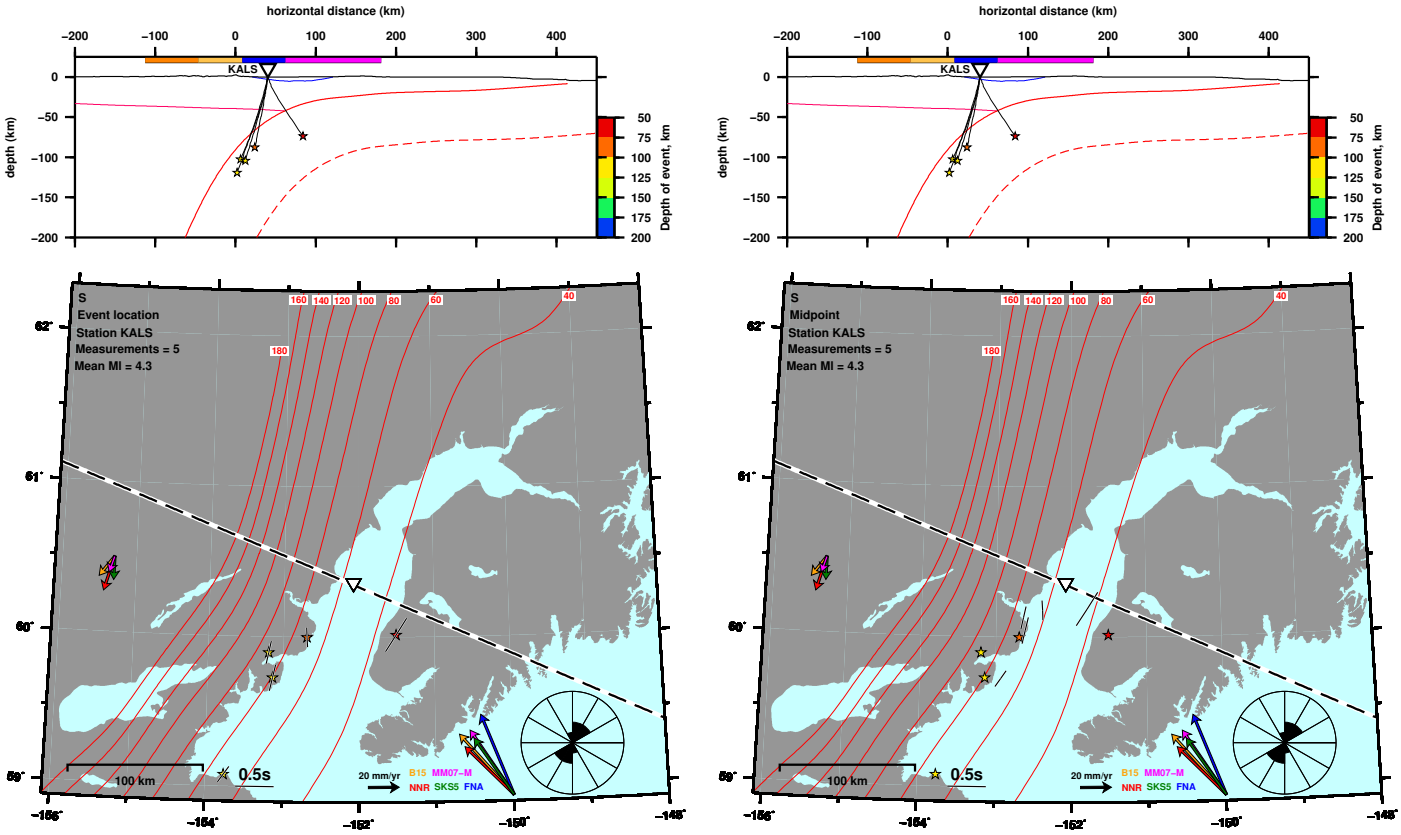


Figure S12: ZE.KALS: Example station 4 out of 5 from west to east on the Redoubt line. KALS displays a trench-parallel pattern and has ray paths that sample the mantle nose. Splitting measurements are plotted at the event location (left) or midpoint projection (right)

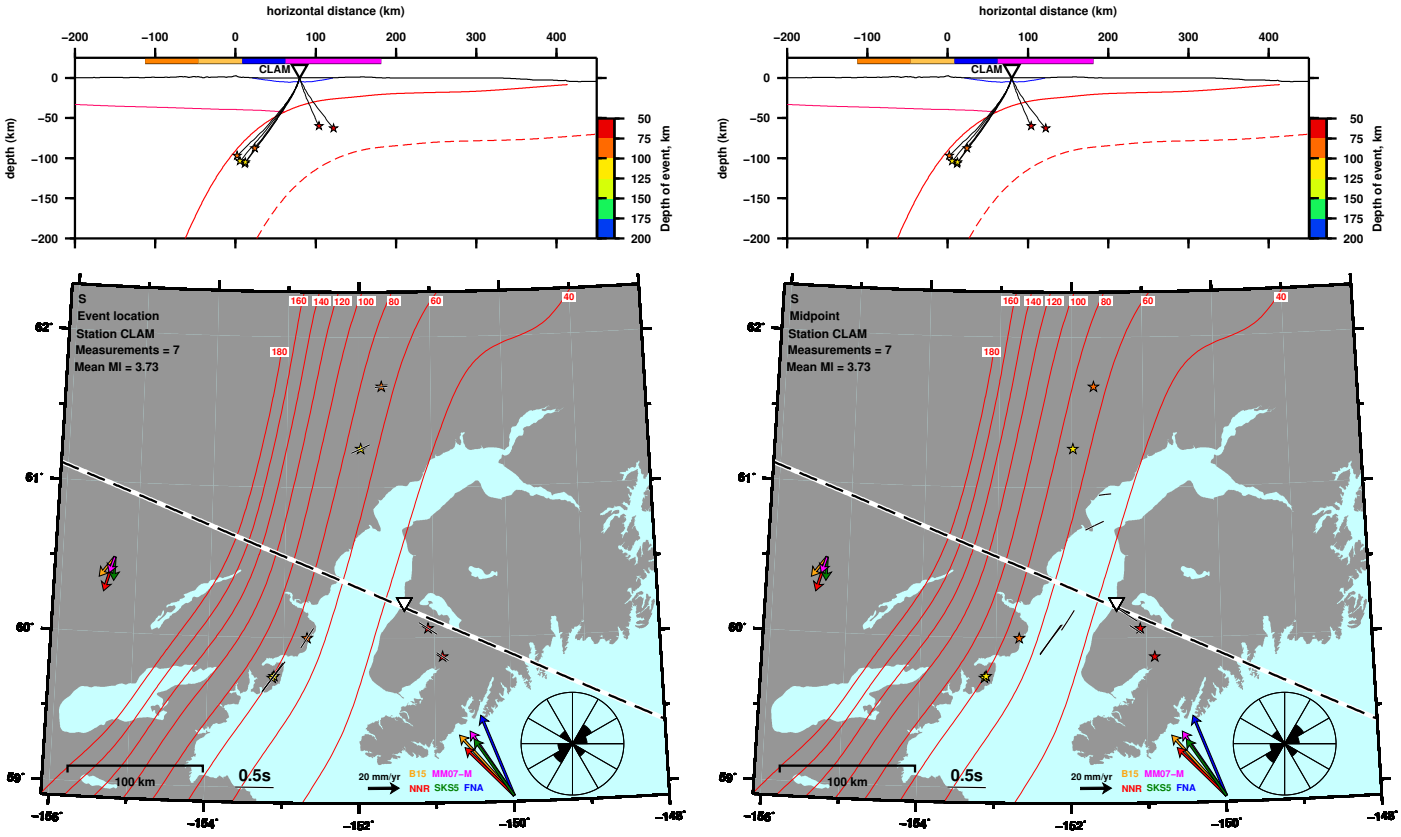


Figure S13: ZE.CLAM: Example station 5 out of 5 from west to east on the Redoubt line. CLAM displays a trench-parallel pattern and has ray paths that (barely) sample the mantle nose. Splitting measurements are plotted at the event location (left) or midpoint projection (right)

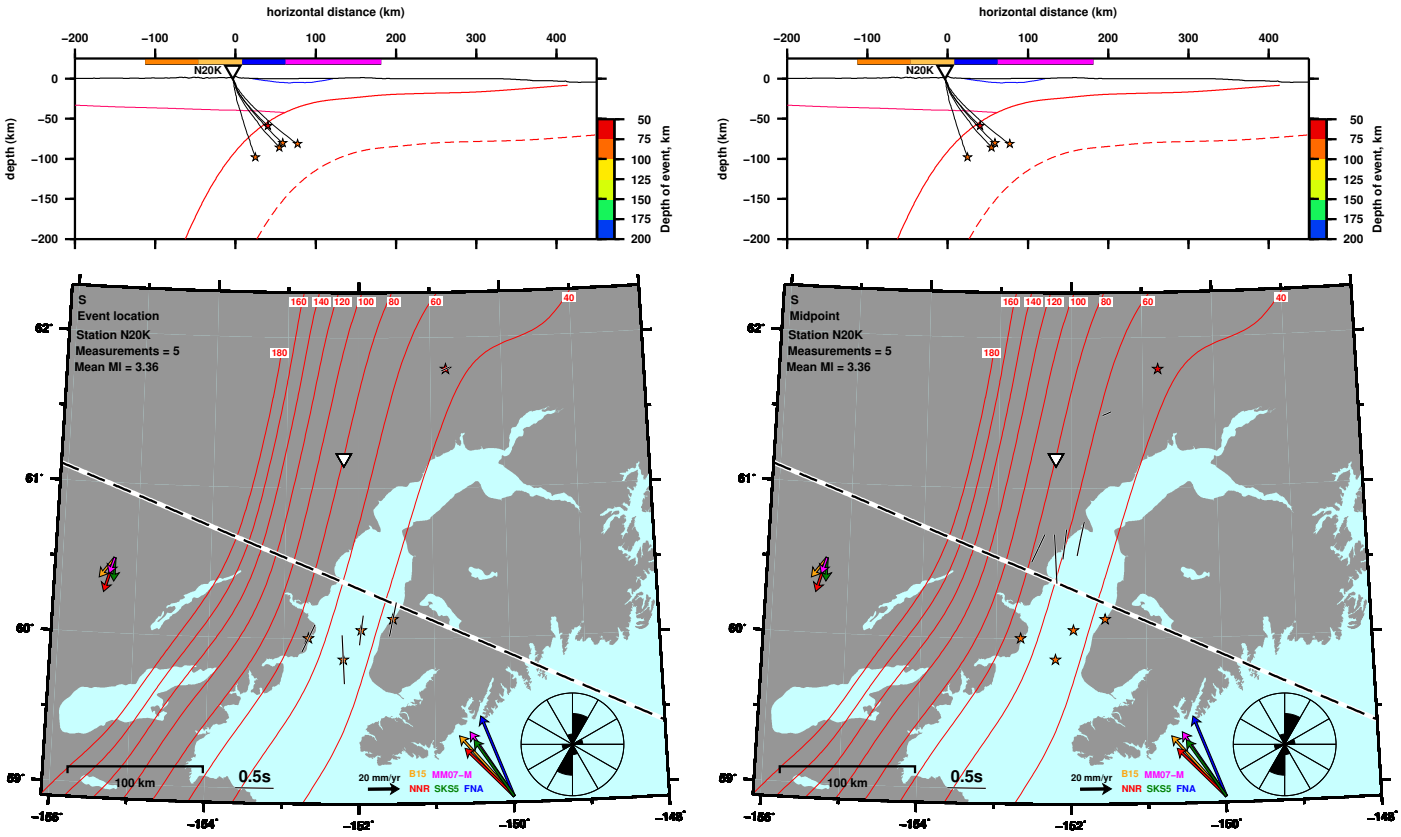


Figure S14: TA.N20K displays a trench-parallel pattern and has ray paths that sample the mantle nose. Splitting measurements are plotted at the event location (left) or midpoint projection (right)

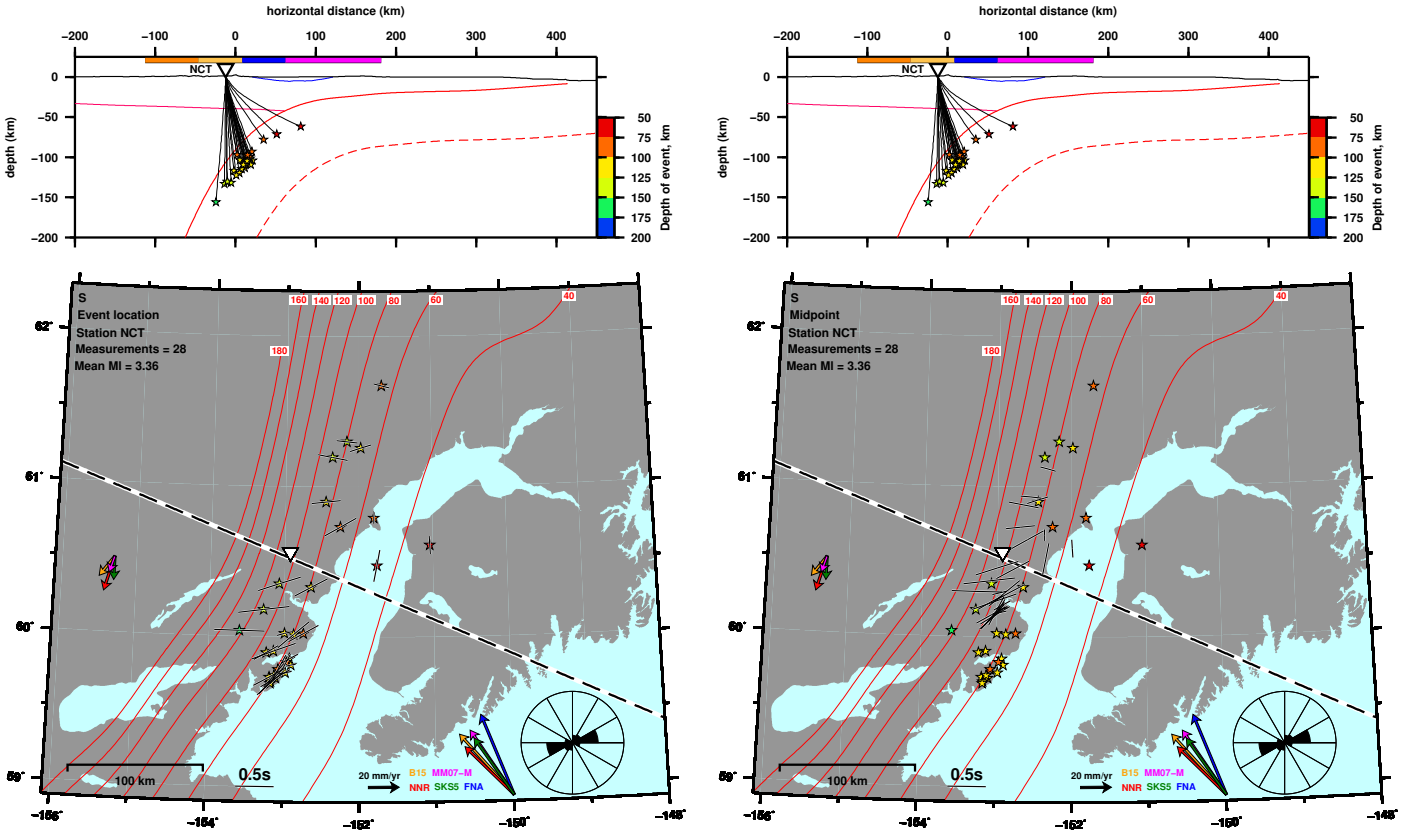


Figure S15: AV.NCT displays a trench-parallel pattern for ray paths that sample the mantle nose and trench-perpendicular for ray paths that sample the wedge. Splitting measurements are plotted at the event location (left) or midpoint projection (right)

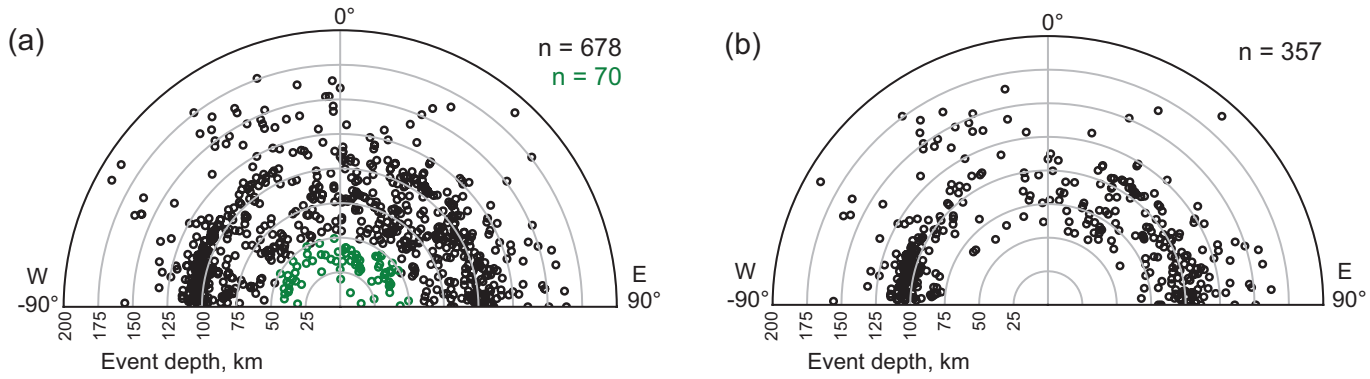


Figure S16: Fast direction as a function of event depth for grade-A local S splitting measurements. In the polar plot, 0° points north and the radial coordinate is event depth, which ranges from 0 to 200 km. (a) All 748 measurements, 70 (green) of which are in the crust. (b) Subset of 357 measurements sampling the mantle wedge.